



Oxygen vacancies in Co_3O_4 promote CO_2 photoreduction

Qi Zhang^a, Pengju Yang^{a,*}, Hongxia Zhang^a, Jianghong Zhao^a, Hu Shi^b, Yamin Huang^c, Hengquan Yang^a

^a School of Chemistry and Chemical Engineering, Shanxi University, Taiyuan 030006, China

^b School of Chemistry and Chemical Engineering & Institute of Molecular Science, Shanxi University, Taiyuan 030006, China

^c State Key Laboratory of Functional Materials for Informatics, Shanghai Institute of Microsystem and Information technology, Chinese Academy of Sciences, Shanghai 200050, China

ARTICLE INFO

Keywords:

CO_2 reduction
Visible light
Oxygen vacancy
Photocatalysis
Cobalt oxide

ABSTRACT

The introduction of oxygen vacancies (OVs) in metal oxides has been proved to be a powerful means for promoting the activation of CO_2 . However, the lack of effective methods for OVs implantation currently hampers the rational design of highly-active CO_2 reduction catalysts. Herein, we reported a novel non-equilibrium photochemical strategy for preparing OV-rich Co_3O_4 at ambient temperature and pressure. Results confirm that the single isolated OV and Co-OV associates are the predominant defect types within Co_3O_4 skeleton. Moreover, the OVs concentration in Co_3O_4 can be tuned over a wide range by merely controlling the light-irradiation time. The experiments and theoretical calculations reveal that the OVs can promote the adsorption/activation of CO_2 and water, while considerably lowering the free energy barrier for COOH^* formation, thereby accelerating the reaction kinetics. The OV-rich Co_3O_4 displays a 26.7-fold improvement in CO_2 reduction activity over the OV-poor Co_3O_4 . The turnover frequency of Co atoms in OV-rich Co_3O_4 reaches 3.754 s^{-1} , which is one of the best reported catalysts for CO_2 photoreduction to date. Moreover, we also successfully synthesize a series of defect-rich metal oxides and metal sulfides using this photochemical method, such as TiO_2 , Fe_2O_3 , CuO , Mn_3O_4 , CeO_2 , V_2O_5 , MoO_3 , ZrO_2 , Bi_2O_3 , MoS_2 , MnS , CdS , NiS_2 - Ni_3S_4 and Bi_2S_3 - BiS_2 , which suggests its universality. We believe this photochemical method developed herein greatly enriches the knowledge for the synthesis of defective nanocrystals under mild synthesis conditions. Importantly, the relationship between the OVs and the CO_2 reduction performance has been established by various characterizations, which may guide the design of highly-efficient catalysts for CO_2 photofixation.

1. Introduction

Converting CO_2 into chemicals and fuels via a photocatalytic process is thought to be a promising path to mitigate the energy crisis [1,2]. Recently, Co_3O_4 catalyst has been considered as a potential candidate for CO_2 conversion, but the intrinsic activity of Co_3O_4 catalyst remains moderate [3–5]. From both theoretical and experimental perspectives, CO_2 activation is considered as a key step during the conversion of CO_2 [6]. To improve the conversion efficiency of CO_2 , it is important to rationally design a highly active and robust Co_3O_4 catalyst, which can efficiently capture CO_2 molecules and activate the stable $\text{C}=\text{O}$ nonpolar bonds [7–9].

In principle, the introduction of OVs in Co_3O_4 catalysts could promote the adsorption and activation of CO_2 because the defects can change the spatial charge distribution and thus induce surface

polarization [10]. Moreover, the defect sites can act as charge-carrier trapping sites. Consequently, the defects will trap photogenerated charges, and thus further enable the activation of CO_2 by transferring photogenerated electrons to the antibonding orbitals of adsorbed CO_2 [11,12]. However, the generation of OVs is difficult to control by conventional chemical reduction methods, and these methods usually require high temperature and are time consuming [13,14]. It has been confirmed that low-temperature synthesis routes could in-situ retain abundant OVs during the synthesis processes of metal oxides [15,16]. However, metal oxides prepared by conventional low-temperature routes mostly exhibit amorphous structure [17]. Despite continuous efforts, it remains a challenge to prepare OV-rich metal oxides with well-defined crystal structure under low-temperature reaction conditions.

Photochemistry is ubiquitous in the ambient environment and of

* Corresponding author.

E-mail address: yangpengju10@mails.ucas.ac.cn (P. Yang).

<https://doi.org/10.1016/j.apcatb.2021.120729>

Received 3 July 2021; Received in revised form 11 September 2021; Accepted 13 September 2021

Available online 17 September 2021

0926-3373/© 2021 Elsevier B.V. All rights reserved.

major importance for natural chemical processes in all phases of matter [18]. When photon energy is comparable to the energy of the chemical bond, high-energy photons can break and reconstruct such bond even at room temperature, thereby inducing the formation of nanocrystals [18]. Moreover, under the conditions required for reaction, thermal chemistry always moves toward thermodynamic equilibrium, but photochemistry can move away from it. The non-equilibrium nature of photochemistry allows for the generation of defect-rich but stable nanocrystals. Recently, our group have synthesized defective carbon nitride polymer and nanocarbons by a room-temperature photochemical approach, suggesting that photochemistry has potential to emerge as a new tool for functional materials fabrication [19,20]. Therefore, it is expected to prepare an OV-rich Co_3O_4 nanocrystal by photochemistry. However, to the best of our knowledge, there is no report on the fabrication of OV-rich Co_3O_4 nanocrystal by photochemistry. Additionally, as a key fundamental issue in catalysis, the defect structure-performance relationship has been pursued for a long time. Yet, it remains elusive for a majority of reactions, such as CO_2 reduction reaction. Therefore, it is highly desirable to establish the defect structure-performance relationship at the atomic level.

Herein, we successfully synthesized OV-rich Co_3O_4 catalysts by a photochemical method at ambient temperature and pressure (30 °C and 1 atm) for the first time. The OVs concentration of Co_3O_4 prepared by this photochemical approach is obviously higher than that of Co_3O_4 prepared by conventional thermochemical approach. Besides, the OVs concentration can be tuned over a wide range by governing the UV-irradiation time. As expected, the OV-rich Co_3O_4 catalyst exhibits excellent activity for CO_2 reduction. Moreover, using this photochemical method, we also successfully synthesized a diverse range of defect-rich metal oxide and metal sulfide nanocrystals, such as TiO_2 , Fe_2O_3 , CuO , Mn_3O_4 , CeO_2 , V_2O_5 , MoO_3 , ZrO_2 , Bi_2O_3 , MoS_2 , MnS , CdS , NiS_2 - Ni_3S_4 and Bi_2S_3 - BiS_2 . Importantly, the intrinsic relationship between the OVs and the catalytic activity toward CO_2 reduction has been established by various characterizations and DFT calculations, which may guide the rational design of efficient CO_2 reduction catalysts.

2. Experimental

2.1. Preparation of OVs-rich Co_3O_4

Firstly, 0.05 g cobalt acetylacetonate was dissolved in water/ethanol solution (200 mL water, 20 mL ethanol). And then, the solution was irradiated by a high-pressure Hg lamp (300 W) at 30 °C. After reaction, the precipitated solids are filtered and washed with water. Finally, the solids were dried at 80 °C for 12 h. The obtained Co_3O_4 after 6, 12 and 18 h light-irradiation reaction were denoted as Co_3O_4 -6, Co_3O_4 -12 and Co_3O_4 -18, respectively. The photograph of Co_3O_4 -12 aqueous solution is shown in Fig. S1. The suspension of Co_3O_4 -12 showed the Tyndall phenomenon, suggesting the good dispersion and high stability.

2.2. Preparation of Co_3O_4 -T

The Co_3O_4 -T was prepared by conventional thermal decomposition of cobalt nitrate. Typically, 1.5 g cobalt nitrate was put into a quartz boat and calcined at the temperature 573 K (2 K/min heating rate) for 5 h in air. After cooling to room temperature, the obtained catalyst was denoted as Co_3O_4 -T.

2.3. Characterization

X-ray diffraction (XRD) measurements were performed on Bruker D8 Advance diffractometer. Raman spectra were recorded on a LABRAM-HR in plus laser Raman spectrometer. N_2 adsorption-desorption isotherms were collected on a Micromeritics ASAP 2020. X-ray photoelectron spectroscopy (XPS) was carried out on Thermo ESCALAB 250 spectrometer. Shimadzu UV-3600 UV-Vis spectrophotometer was

employed for UV-vis absorption spectroscopy analysis. Micromeritics ASAP 2020 was used for CO_2 adsorption test. Fluorescence (PL) and time-resolved PL spectra were analyzed by using a FLSP 920 fluorescence spectrophotometer. A FEI Talos 200 F microscope was used for morphology analysis. A JES FA200 electron paramagnetic resonance (EPR) was used for oxygen vacancies analysis. Electrochemistry experiments were conducted for hydrogen evolution catalysis analysis (Pt sheet as the counter electrode, saturated calomel electrode as the reference electrode). A Nano Scope IV instrument was used to analyse the thickness of samples. Scanning electron microscopy (SEM) images were investigated on a JSM-7001 F microscope. The PAS was measured by a fast-slow coincidence ORTEC system. A ^{22}Na source with 20 μCi strength was used as a positron source (time resolution of 190 ps). A Micromeritics Chemisorption Analyzer was used for CO_2 temperature desorption analysis. The X-ray absorption near-edge structure (XANES) and extended X-ray absorption fine structure (EXAFS) of the sample at Co-edge was collected at the Beamline of TPS44A1 in National Synchrotron Radiation Research Center (NSRRC), Taiwan.

2.4. Photocatalytic reaction and quantum yield measurements

The $[\text{Ru}(\text{bpy})_3]\text{Cl}_2 \cdot 6\text{H}_2\text{O}$ (12 mg), Co_3O_4 catalyst (1 μg) and solvent [6 mL, H_2O /acetonitrile/TEOA = 2:3:1 (vol/vol)] were added to the flask reactor (Because the solubility of CO_2 in acetonitrile highly reaches 0.27 M, thus acetonitrile is employed as a solvent medium for promoting CO_2 reduction reaction kinetics.). After vacuum degassing, the reactor was filled with high-pure CO_2 (99.999%, 1 atm). A 300 W Xenon lamp ($\lambda \geq 420\text{ nm}$) was employed as light source. The reaction temperature was controlled at 30 °C by a cooling water system. The zeta potential of Co_3O_4 -12 obtained at pH 7 is -35.8 mV (Fig. S2). Hence, the Co_3O_4 -12 can adsorb $\text{Ru}(\text{bpy})_3^{2+}$ by electrostatic interaction. A gas chromatography (FID detector) was used for products analysis. The $^{13}\text{CO}_2$ experiment was carried out under the same reaction conditions and a gas chromatography-mass spectrometry was employed to analyse the generated ^{13}CO .

The quantum yield (QY) for CO_2 reduction was measured using 450 nm LED lamp with band pass filter of 450 nm with an irradiation area of 0.196 cm^2 . The light intensity was 16.4 mW cm^{-2} .

$$\text{QY} = \frac{\text{Ne/Np} \times 100\%}{2\text{ M NAhc/Spt}\lambda \times 100\%}$$

where M, S, P, T and λ are the amount of CO, light irradiation area, light density, reaction time, and light wavelength, respectively.

The turnover frequency (TOF) is calculated on the basis of the surface Co atoms. The surface area of per Co_3O_4 unit cell is 0.652864 nm^2 . The unit cell of Co_3O_4 contains 24 Co atoms. Avogadro constant (NA) = 6.02×10^{23} .

$$\text{Surface Co atoms (mol)} = \frac{\text{BET surface area}}{\text{Surface area of per unit cell} \times \text{NA}} \times 24$$

Thus, the surface Co atom amounts of Co_3O_4 -6, Co_3O_4 -12, Co_3O_4 -18 and Co_3O_4 -T per micro-gramme are 0.00274, 0.00219, 0.00371 and 0.00103 μmol .

$$\text{TOF} = \frac{\text{Generated amount of syngas per hour}}{\text{Amount of surface Co atoms}}$$

2.5. Computational details

Density functional theory (DFT) calculations were performed based on the Perdew–Burke–Ernzerhof (PBE) form of generalized gradient approximation functional by employing the Vienna ab-initio simulation package (VASP) [21,22]. To describe the interactions between valence electrons and ion cores, the Blöchl's all-electron-like projector augmented wave (PAW) method was employed [23,24]. A kinetic cutoff energy of 400 eV was applied for the plane wave basis set. Brillouin zone integration was approximated by a $3 \times 2 \times 1$ k-points using the

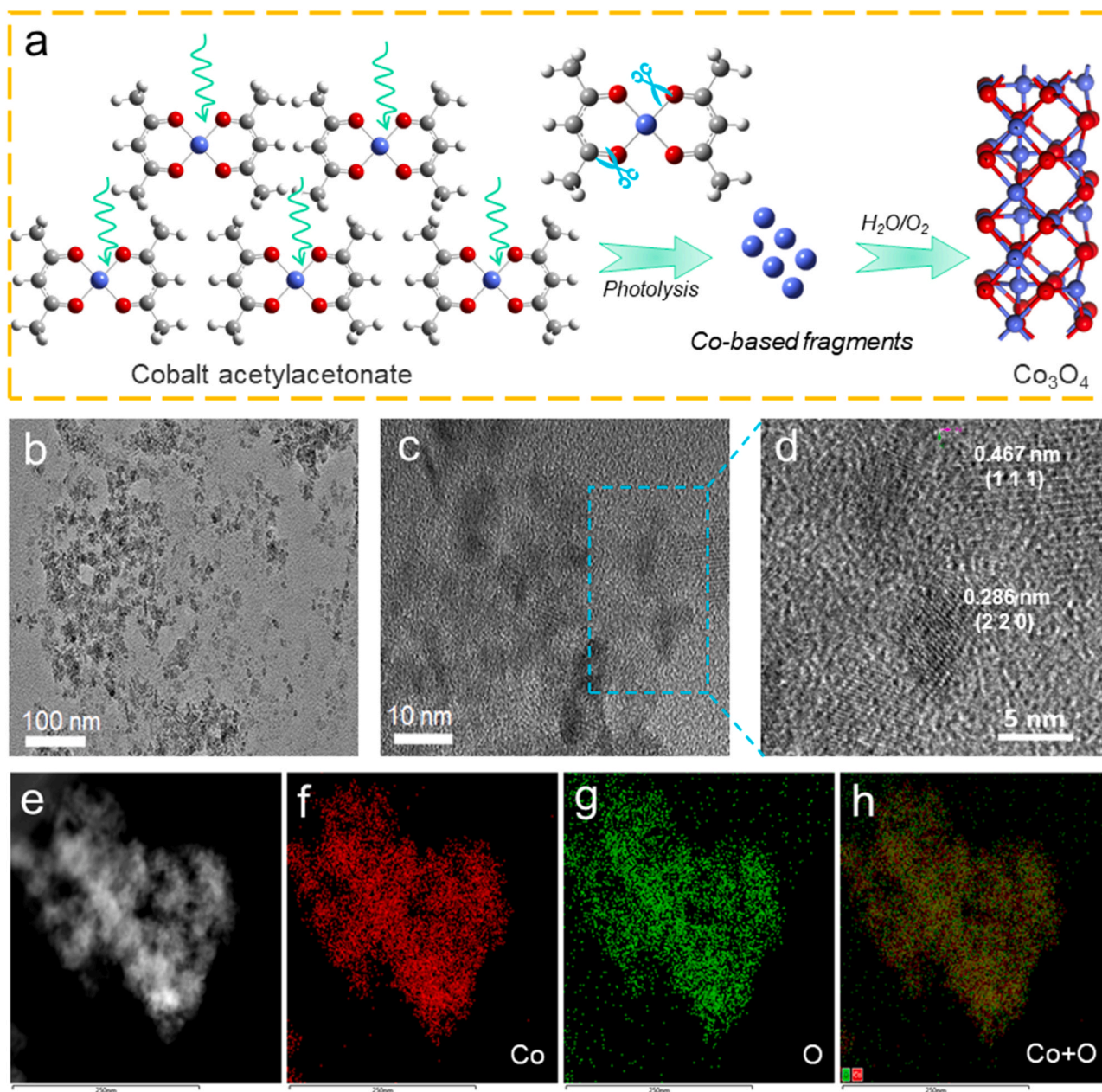


Fig. 1. Structural characterizations. (a) The schematic illustration of OV-rich Co_3O_4 synthesis, (b–d) TEM and HRTEM images of Co_3O_4 -12 and (e–h) Elemental mappings of Co_3O_4 -12.

Monkhorst-Pack grid [25]. Geometries were optimized until the energy was converged to 1.0×10^{-6} eV/atom and the force was converged to be 0.01 eV/Å. To avoid the periodic interactions for all the structures, a vacuum layer as large as 20 Å is used along the c direction normal to the surface. In current study, the zero-point energy (ZPE) and entropy correction were involved, the ΔG by the following equation, $\Delta G = \Delta E + \Delta \text{ZPE} - T\Delta S$.

3. Results and discussion

3.1. Synthesis and characterization

UV–vis absorption spectrometry was used to monitor the formation of Co_3O_4 nanocrystal. As revealed in Fig. S3, the characteristic absorption of cobalt acetylacetonate gradually decreases with increasing the UV-irradiation time (high-pressure Hg lamp), which suggests that cobalt acetylacetonate can be consumed by photolysis. After UV-irradiation of

6 h, the characteristic absorption of cobalt acetylacetonate disappears. At the same time, some new absorption bands are observed, which matches well with the optical features of Co_3O_4 , reflecting the formation of Co_3O_4 . A proposed process for the OV-rich Co_3O_4 synthesis by photochemistry is shown in Fig. 1a.

The Co_3O_4 nanocrystals prepared by different UV-irradiation time are denoted as Co_3O_4 -x (x = 6, 12 and 18 h). Fig. 1b shows the transmission electron microscope (TEM) image of the as-prepared Co_3O_4 -12 sample. The Co_3O_4 -12 displays particle-like morphology with a size of less than 20 nm. The high-resolution TEM (HRTEM) image suggests the crystalline nature of Co_3O_4 -12 (Fig. 1c and d). The lattice fringes with interplanar spacing of 0.286 and 0.467 nm can be attributed to the (2 2 0) and (1 1 1) planes of Co_3O_4 , respectively [26]. Elemental mappings suggest that the Co and O atoms are uniformly distributed over the entire scanned areas (Fig. 1e–h). The TEM and HRTEM images of Co_3O_4 -6 and Co_3O_4 -18 are shown in Figs. S4 and S5. The Co_3O_4 -6 and Co_3O_4 -18 display similar morphology with the Co_3O_4 -12. This suggests

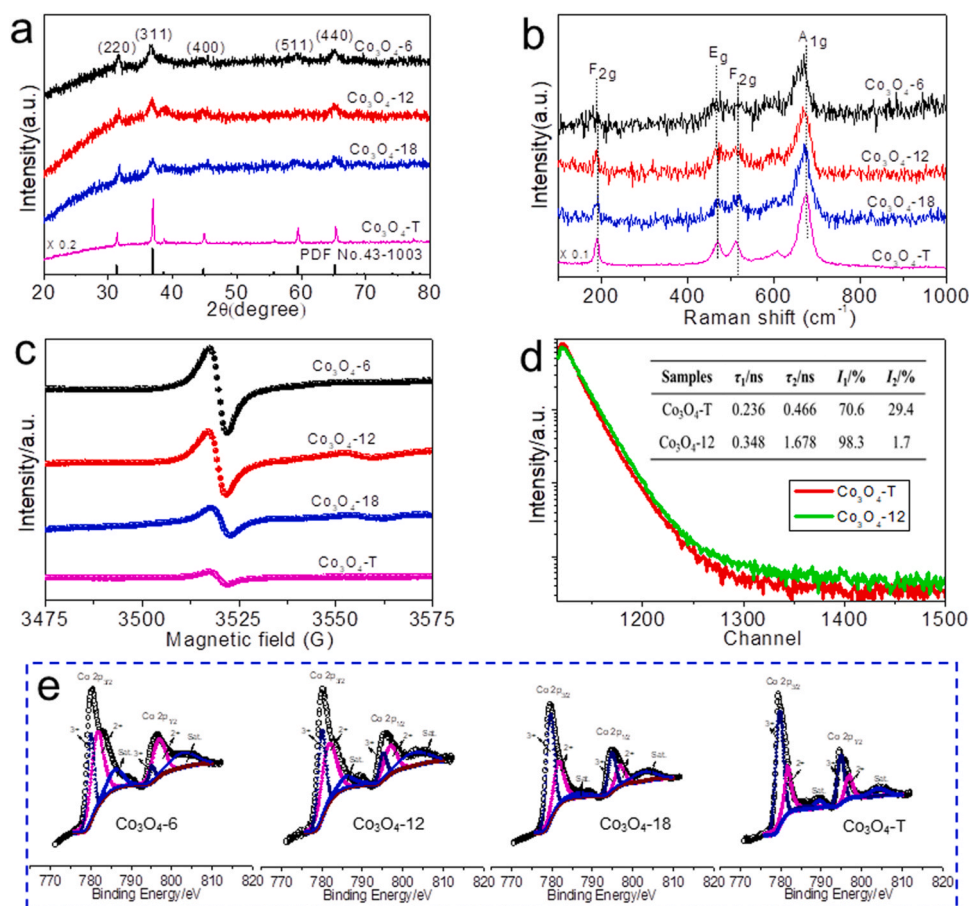


Fig. 2. Structural characterizations. (a) XRD, (b) Raman, (c) EPR and (e) High-resolution XPS spectra of the Co 2p for all samples, and (d) PAS lifetimes of Co₃O₄-T and Co₃O₄-12.

that this photochemical method has little influence on the morphology progression, which probably relates to its low synthesis temperature. UV–vis absorption spectra of Co₃O₄-6, Co₃O₄-12 and Co₃O₄-18 are exhibited in Fig. S6. The TEM and HRTEM images of Co₃O₄ prepared by thermochemical method (denoted as Co₃O₄-T) are shown in Fig. S7.

X-ray diffraction (XRD) profiles of all samples are revealed in Fig. 2a. All the diffraction peaks can be indexed to a standard PDF card of spinel Co₃O₄ phase (PDF No. 43-1003) [27]. Moreover, we observed that the (2 2 0) peak of the Co₃O₄ synthesized by photochemical strategy shows a slight shift, which can be attributed to the existence of rich OV. Raman spectra of all samples are shown in Fig. 2b. Characteristic peaks at about 193, 473, 520 and 675 cm⁻¹ correspond to the F_{2g}, E_g, F_{2g} and A_{1g} modes of Co₃O₄, in agreement with the XRD results [26,27]. The surface areas of Co₃O₄-6, Co₃O₄-12, Co₃O₄-18, and Co₃O₄-T determined by N₂ adsorption-desorption isotherms are 61.3, 36.2, 45.5, and 17.1 m²/g, respectively (Fig. S8). The relative high surface areas of Co₃O₄ prepared from this photochemical method can be ascribed to the low synthesis temperature.

X-ray photoelectron spectroscopy (XPS) was first performed to determine the presence of OV within Co₃O₄. The peaks at 529.8 ± 0.1 (O1 peak), 531 ± 0.2 (O2 peak), and 533.4 ± 0.2 eV (O3 peak) can be ascribed to the Co-O, OV and hydroxyl species, respectively (Fig. S9) [28–30]. The relative contents of Co-O, OV and hydroxyl species of all samples are summarized in Table S1. Obviously, the OV concentration of Co₃O₄-6 is higher than that of Co₃O₄-T, suggesting that the photochemical synthesis is an effective strategy for the fabrication of OV-rich Co₃O₄. Besides, we observed that the OV concentrations in the Co₃O₄ gradually decrease by increasing the UV-irradiation time, which reflects the controllability of this method. The decreased OV concentration

probably can be attributed to the gradually enhanced crystallinity of Co₃O₄ caused by the increase of reaction time [31].

As known, the OV in Co₃O₄ are often accompanied by the coordination unsaturated Co sites. Hence, we analysed the XPS Co 2p spectra of all samples (Fig. 2e). The binding energy values at around 780 ± 0.2 eV and 796 ± 0.2 eV correspond to Co 2p_{3/2} and Co 2p_{1/2}, respectively [28–30]. The Co 2p_{3/2} and Co 2p_{1/2} peaks can be mainly fitted by two regions of Co³⁺ and Co²⁺ [28–30]. The peaks at 781.7 ± 0.2 and 796.8 ± 0.2 eV can be ascribed to Co²⁺, while the other two peaks at 779.9 ± 0.2 and 795.0 ± 0.2 eV correspond to Co³⁺. The relative contents of Co³⁺ and Co²⁺ for all samples are calculated and shown in Table S2. The atomic ratios of Co²⁺/Co³⁺ for Co₃O₄-6, Co₃O₄-12, Co₃O₄-18 and Co₃O₄-T are 1.17, 0.97, 0.66 and 0.53, respectively. The theoretical ratio of Co²⁺/Co³⁺ for perfect Co₃O₄ is 0.5. The Co²⁺/Co³⁺ ratios for the Co₃O₄-6, Co₃O₄-12 and Co₃O₄-18 are obviously higher than the theoretical value (Table S2), suggesting more Co²⁺ present in the Co₃O₄, that is, OV are generated, which is consistent well with the observation of O 1s spectra. The Co²⁺/Co³⁺ ratio for Co₃O₄-T is slightly higher than the theoretical value, advising its low OV concentration. Electron paramagnetic resonance (EPR) spectra were also employed to analyse the formation of OV, as shown in Fig. 2c. All samples display an EPR signal at g = 2.001, which can be attributed to the OV signal of Co₃O₄ [32]. The EPR intensity increases with the increase of OV concentration [33], validating the observation of XPS.

To further verify the existence of OV, synchrotron extended X-ray absorption fine structure (EXAFS) and X-ray absorption near edge structure (XANES) were performed. As shown in Fig. 3a, the spectral profiles of Co K-edge XANES of Co₃O₄-T (OV-poor Co₃O₄) and Co₃O₄-12 (OV-rich Co₃O₄) are similar to that of standard Co₃O₄ rather than those

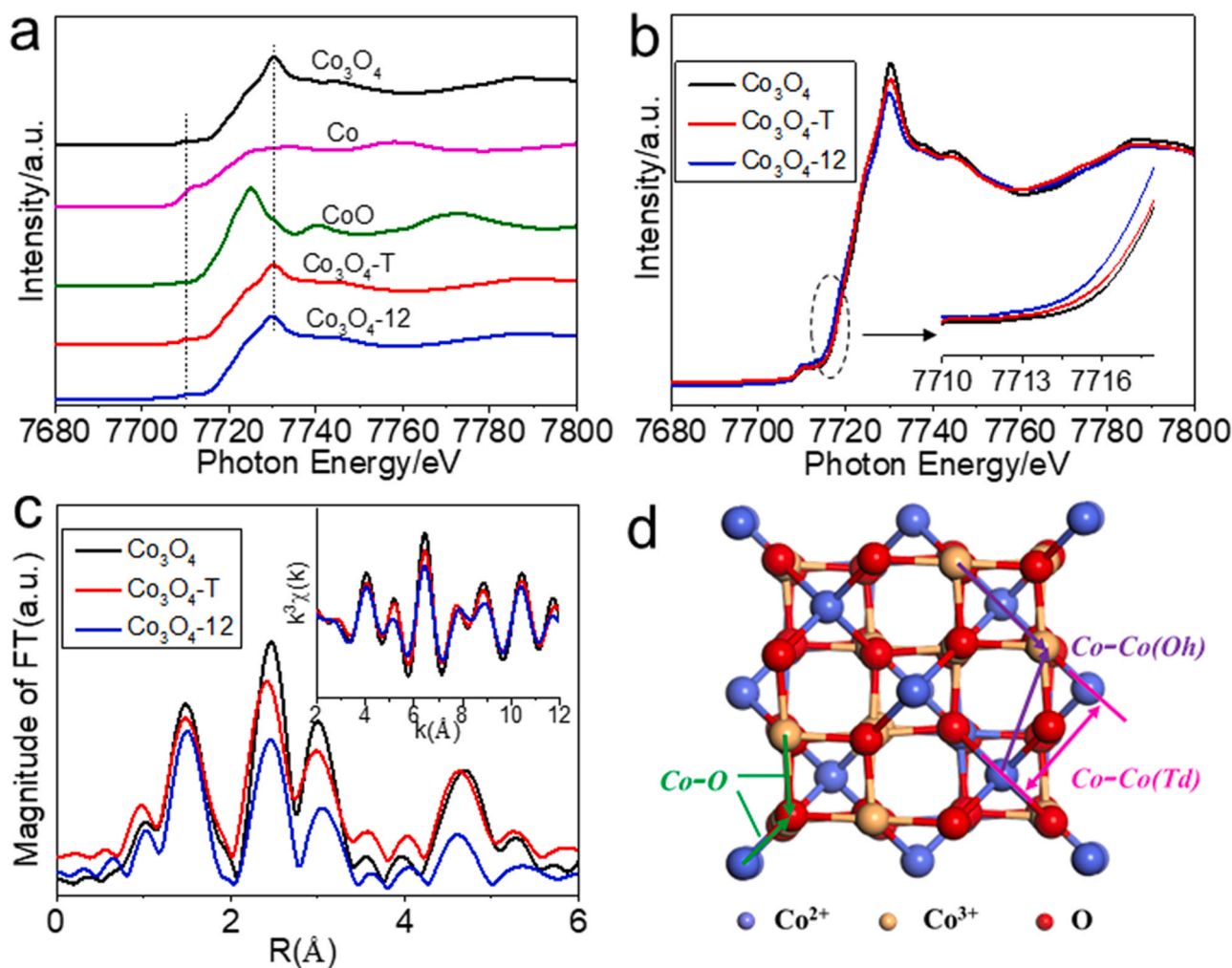


Fig. 3. Structural characterizations. (a, b) Co K-edge XANES spectra of $\text{Co}_3\text{O}_4\text{-T}$ and $\text{Co}_3\text{O}_4\text{-12}$, (c) Co K-edge EXAFS. Inset is the Fourier-transform EXAFS oscillations. (d) Structure configurations of Co_3O_4 .

of the Co foil and CoO, suggesting that the average Co oxidation state of Co_3O_4 is different from those of CoO and Co [34,35]. Detailed comparison of the main peak is presented in Fig. 3b. The $\text{Co}_3\text{O}_4\text{-12}$ exhibits a lower intensity, which can be associated with a lower oxidation state. Moreover, compared to the case of standard Co_3O_4 and OV-poor Co_3O_4 ($\text{Co}_3\text{O}_4\text{-T}$), a shift to lower energy was observed in OV-rich Co_3O_4 ($\text{Co}_3\text{O}_4\text{-12}$), confirming a lower Co oxidation state of $\text{Co}_3\text{O}_4\text{-12}$ [34,35]. The Co K-edge Fourier-transform data of standard, OV-poor and OV-rich Co_3O_4 are displayed in Fig. 3c. The first peak is originated from the Co-O bonds. The second and third peaks can be ascribed to the two adjacent octahedrally (Oh) and tetrahedrally (Td) Co-Co sites, respectively (Fig. 3d) [35]. Compared with the standard Co_3O_4 and OV-poor Co_3O_4 ($\text{Co}_3\text{O}_4\text{-T}$), a lower Co-O Fourier-transform intensity can be found in the $\text{Co}_3\text{O}_4\text{-12}$. This result authorizes that the $\text{Co}_3\text{O}_4\text{-12}$ has a lower coordination number (rich OVs), which is well supported by the calculation results of Co-O coordination numbers (Fig. S10 and Table S3) [34,35].

To determine the structural features of OVs, positron annihilation spectroscopy (PAS) was performed. The PAS spectra of the $\text{Co}_3\text{O}_4\text{-T}$ and $\text{Co}_3\text{O}_4\text{-12}$ are shown in Fig. 2d. The PAS lifetimes are summarized in Fig. S11 and Table S4. The shorter lifetime component (τ_1) can be ascribed to positron annihilation as trapped at the small OVs (single isolated OV and Co-OV associates) [36,37]. The longer lifetime component (τ_2) is attributed to positron annihilation in the large OV clusters [36,37]. The average lifetime represents the defective state of the sample as a whole. It is to be noted that the average lifetime of the $\text{Co}_3\text{O}_4\text{-12}$ (371 ps) is obviously longer than that of the $\text{Co}_3\text{O}_4\text{-T}$

(303.3 ps), which suggests that the $\text{Co}_3\text{O}_4\text{-12}$ has a higher OVs concentration [38,39]. Besides, the relative intensity (I) provides information on the relative concentration of the defects [40]. The relative intensity (I_1) of the $\text{Co}_3\text{O}_4\text{-12}$ highly reaches 98.3%, signifying that the single isolated OV and Co-OV associates are the predominant defect types in the $\text{Co}_3\text{O}_4\text{-12}$ skeleton [36,37,40].

3.2. Photocatalytic activity test

Motivated by the high OVs concentration, we investigated the catalytic performance of Co_3O_4 toward CO_2 photoreduction with $[\text{Ru}(\text{bpy})_3]\text{Cl}_2 \cdot 6\text{H}_2\text{O}$ as sensitizer (denoted as Ru dye) under visible light ($\lambda \geq 420 \text{ nm}$). As expected, the as-prepared Co_3O_4 can catalyze CO_2 -to- CO reduction (hydrogen as a byproduct). As shown in Fig. 4a, the $\text{Co}_3\text{O}_4\text{-12}$ shows the highest activity for syngas production ($\text{CO} + \text{H}_2$) among all samples and exhibits good stability (Fig. S12). The syngas yield of $\text{Co}_3\text{O}_4\text{-12}$ is 26.7 times higher than that of $\text{Co}_3\text{O}_4\text{-T}$. The control experiments are shown in Table S5. When the reaction was performed without the $\text{Co}_3\text{O}_4\text{-12}$ catalyst, only trace H_2 was detected. Without light irradiation, no product was observed. Under Ar atmosphere, we only observed H_2 generation. These findings suggest that catalyst, light irradiation and CO_2 are essential for CO_2 reduction reaction. Besides, $^{13}\text{CO}_2$ reduction experiment was employed to determine the origin of CO. As revealed in Fig. 4b, an obvious ^{13}CO signal ($m/z = 29$) was witnessed, confirming that the generated CO is from CO_2 reduction ($m/z = 45$ corresponding to $^{13}\text{CO}_2$). In addition, the effect of $\text{Co}_3\text{O}_4\text{-12}$

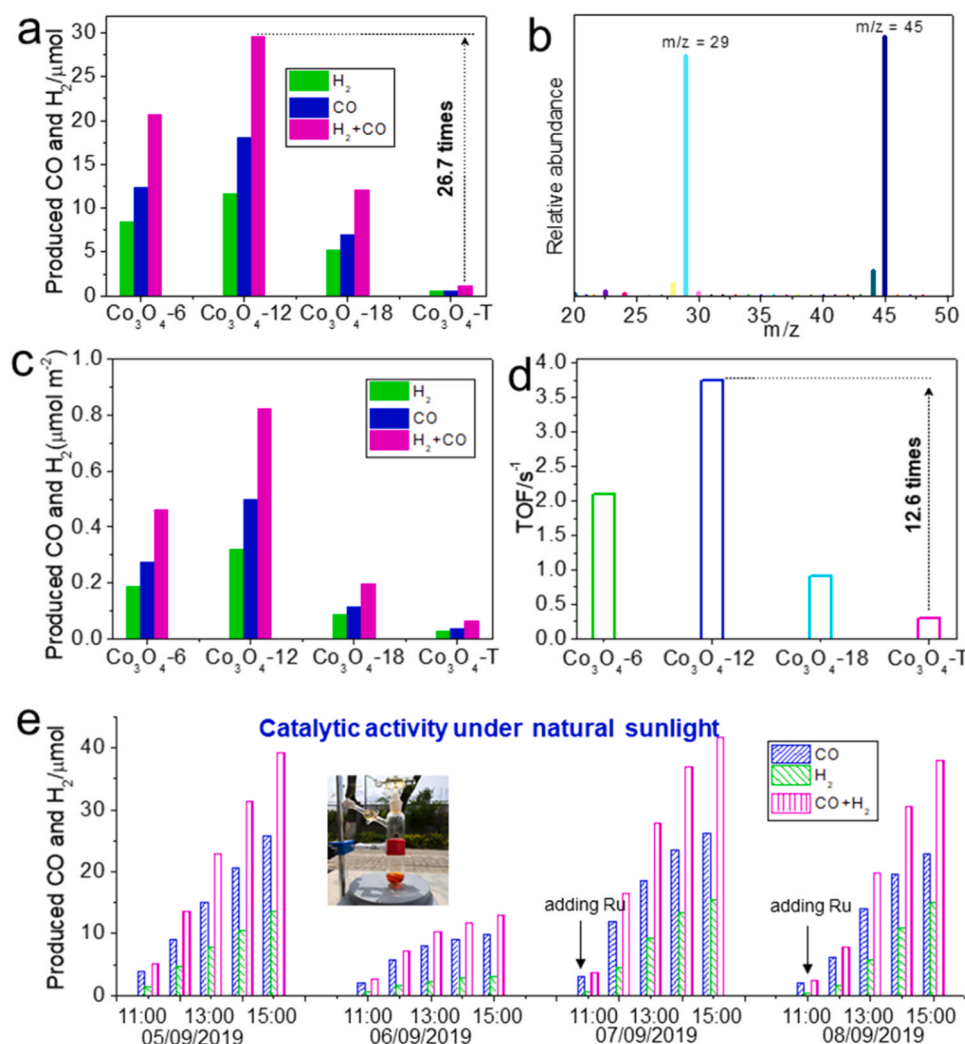


Fig. 4. Catalytic performances of the Co₃O₄ toward CO₂ reduction. (a) Photocatalytic activities of all samples ($\lambda \geq 420$ nm; 1 h reaction), (b) ¹³CO₂ isotope labelling experiment, (c) Specific activities and (d) TOF values of all samples, (e) Catalytic activity of the Co₃O₄-12 under natural sunlight irradiation.

amount on photocatalytic performance was estimated (Fig. S13). When the amount of catalyst is 12 μg, the yield of CO reaches a maximum value of 51.7 μmol together with a H₂ evolution of 35.4 μmol (1 h reaction). With the further increase of catalyst amount, the catalytic activity began to decrease, which may be related to the increased light scattering and shielding effects of catalyst and the reduced surface area caused by catalyst aggregation.

Due to the excellent catalytic activity of Co₃O₄-12, we studied its catalytic performance under natural sunlight irradiation. As shown in Figs. 4c and S14, the Co₃O₄-12 can efficiently drive CO₂ reduction under natural sunlight irradiation. Moreover, the catalytic activity of Co₃O₄-12 can be rejuvenated when extra Ru dye is added into the reaction solution (there exists dye sensitizer degradation during the photocatalytic processes) [41], suggesting the good stability of Co₃O₄-12 catalyst. After a reaction time of 20 h, 132 μmol syngas was produced, suggesting that the Co₃O₄-12 catalyst displays huge potential for solar-to-fuels synthesis under natural solar conditions. To collect the used catalysts more efficiently, we have employed two larger reactors to amplify the reaction and have analysed the XRD, EPR, Raman, FTIR and TEM results of Co₃O₄-12 catalyst after reaction (see SI section for detail). As revealed in Fig. S15, the used Co₃O₄-12 shows similar morphology and structure compared with the fresh Co₃O₄-12, suggesting its good stability.

For the production of chemicals from syngas, the tailoring of H₂/CO ratio in syngas is critical [42,43]. Interestingly, we observed that the

H₂/CO ratio could be adjusted over a wide range between 5.86:1 and 0.64:1 by varying CO₂ concentrations (Fig. S16). When the concentration of CO₂ is relatively low, H₂ is more readily evolved. With increasing the concentrations of CO₂, the H₂/CO ratios could be lowered. Moreover, the H₂/CO ratios can be modulated from 0.59:1–4:1 by controlling the water/MeCN ratios (Fig. S17). As known, the initial process of CO₂ reduction (CO₂ to CO₂^{•-}) requires a high activation energy of −1.9 V (pH 7), but proton-assisted can greatly lower the reaction barrier for CO₂ reduction [44]. Therefore, when appropriate amount of water was introduced into MeCN, CO evolution can be promoted, thereby giving a decreased H₂/CO ratio. However, further increasing the amount of water, the H₂/CO ratio began to increase, which may be related to the competitive adsorption of water on catalysts [45]. In addition, we employed carbon nitride (CN), CdS and TiO₂ (P25) as light-harvesting platforms for CO₂ reduction catalysis (Co₃O₄-12 as a catalyst), as shown in Fig. S18. Expectedly, the CN, CdS and TiO₂ photosystems can drive CO₂-to-CO reduction (hydrogen as a byproduct). But their H₂/CO ratios are noticeably different, which may originate from the different band structures and surface properties of CN, CdS and TiO₂ [46]. This observation reflects that the H₂/CO ratios can be further tuned by altering the light-harvesting antennas.

To investigate the interfacial charge transfer between the Co₃O₄ catalyst and Ru dye, steady-state photoluminescence (PL) and time-resolved PL spectra were performed (Fig. S19) [47,48]. The PL

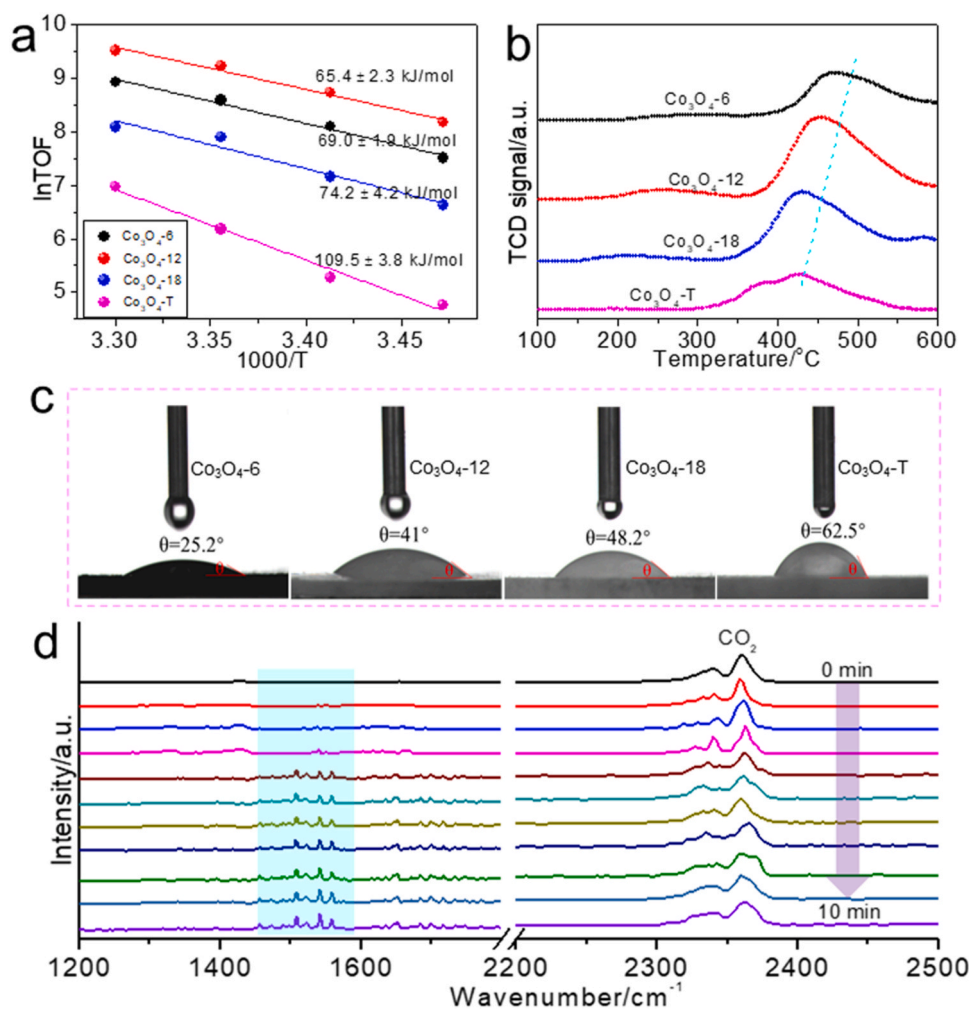


Fig. 5. Characterizations of reaction kinetics and reaction pathway of CO₂ reduction. (a) Arrhenius plots, (b) CO₂-TPD, and (c) CA test of all samples, (d) *In-situ* DRIFTS spectra of Co₃O₄-12 with different light-irradiation time.

intensity of Ru dye became weaker when the Co₃O₄ catalysts were introduced, suggesting that the Co₃O₄ can capture the photogenerated electrons of Ru dye [47,48]. Moreover, the PL lifetimes of Ru/Co₃O₄ systems are lower than that of Ru dye, which further confirms an efficient charge transfer from Ru dye to the Co₃O₄ catalysts, consistent with the results of steady-state PL [49]. Also, we observed that the PL intensities and lifetimes of Ru/OVs-rich Co₃O₄ systems are lower than that of Ru/OVs-poor Co₃O₄ system (Co₃O₄-T), proposing that the OVs can probably function as active sites for trapping photoexcited electrons from Ru dye and thus inhibit the recombination of photoexcited electron-hole pairs of Ru dye [50].

3.3. Relationship between the OVs and the catalytic performance

To establish the relationship between the OVs and the catalytic activity, the specific activities of all Co₃O₄ samples (normalized by surface area) were calculated (Fig. 4d). Obviously, the specific activities of OV-rich Co₃O₄ samples are higher than that of Co₃O₄-T. Moreover, there is no obvious correlation between the surface area and the catalytic activity, suggesting that surface area cannot account for the high activity of OV-rich Co₃O₄. Besides, XRD result confirms that all Co₃O₄ samples have same crystal structure, thereby the effect of crystal structure on its catalytic performance can be ruled out. Furthermore, we calculated the TOF values based on the surface Co atoms. The TOF values of Co₃O₄-6, Co₃O₄-12, Co₃O₄-18, and Co₃O₄-T are 2.098, 3.754, 0.906, and 0.296 s⁻¹, respectively (Table S6 and Fig. 4e). Noticeably, the TOF of

OV-rich Co₃O₄ (such as Co₃O₄-12) is higher than that of OV-poor Co₃O₄-T, suggesting that the OVs play a key role for promoting reaction efficiency. In addition, the Co₃O₄-12, Co₃O₄-6, and Co₃O₄-18 catalysts all show good stability (Figs. S20–S22). The quantum yield (QY) for CO₂ reduction over the Co₃O₄-12 was calculated to be as high as 7.35% at 450 nm. The QY and CO production rates of the representative catalysts are summarized in Table S7. Evidently, the efficiency of Co₃O₄-12 is much higher than those of the reported catalysts, suggesting the effectiveness of this oxygen defect engineering.

The reaction kinetics of all catalysts was revealed in Figs. S23–S26. It can be seen that the syngas yield and TOF gradually increase with the increase of reaction temperature. By fitting the temperature-dependent with the Arrhenius plots, the apparent activation energy (E_a) was obtained (The activation energies do not include the formation processes of electron-hole pairs.) [51]. The E_a values for syngas production over the Co₃O₄-6, Co₃O₄-12, Co₃O₄-18, and Co₃O₄-T catalysts are 69, 65.4, 74.2, and 109.5 kJ mol⁻¹, respectively (Fig. 5a). The Co₃O₄-12 has the lowest activation energy, suggesting faster reaction kinetics and in good agreement with the catalytic performance. The difference in activation energy implies that the properties of Co sites in four cases are different, which can be mainly attributed to the different electronic structure of Co₃O₄ caused by different defect concentration, in agreement well with the DFT calculations (Fig. S27).

Besides, we compared the CO₂ adsorption/activation behaviour of all catalysts by CO₂ adsorption and CO₂ temperature programmed desorption (CO₂-TPD). Fig. S28 shows the CO₂ adsorption capacities of

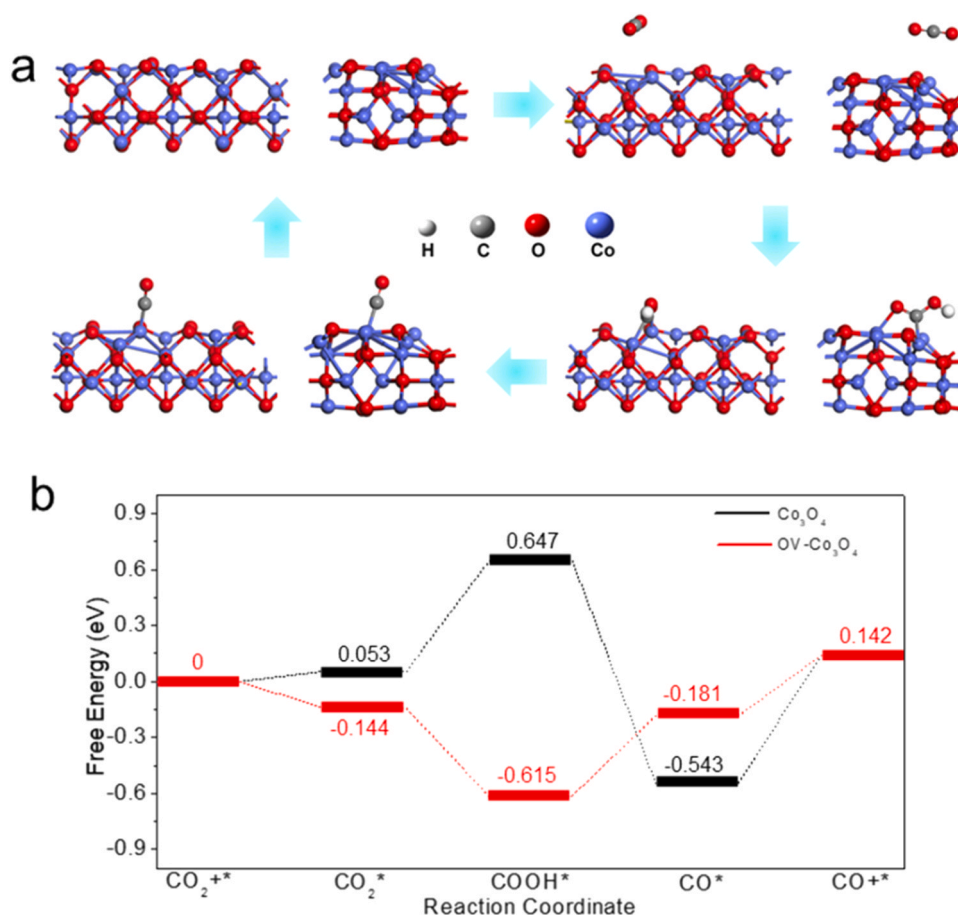


Fig. 6. Analysis of CO₂ reduction mechanism over the Co₃O₄. (a) Possible reaction paths of CO₂-to-CO reduction and (b) Calculated free energy diagram for Co₃O₄ and OV-Co₃O₄.

all samples. It is seen that the CO₂ adsorption capacities increase with the increase of OVs concentration, suggesting that OVs can facilitate CO₂ adsorption. The CO₂-TPD profiles suggest that the Co₃O₄-6, Co₃O₄-12, Co₃O₄-18 and Co₃O₄-T catalysts have different CO₂ desorption behaviour (Fig. 5b). With the increase of OVs concentration, CO₂ desorption signals gradually migrate toward the higher temperature. This result clearly indicates that the OVs modification can strengthen the interaction between the Co₃O₄ and CO₂, which is benefit for promoting the activation and reduction of CO₂ [52]. As known, water adsorption behaviour of catalysts controls the supply of proton source and thus influences the kinetics of CO₂ reduction to some extent. To analyse water adsorption behaviour of catalysts, the contact angle (CA) experiments were performed. As shown in Fig. 5c, the CA values gradually decrease with the increase of OVs concentrations, signifying that OVs can also encourage water adsorption. In principle, the tight interaction between catalysts and substrate molecules can facilitate the activation of reactants, thereby accelerating the reaction kinetics. Compared with the OVs-poor Co₃O₄, the OVs-rich Co₃O₄ catalysts show stronger interaction with substrate molecules, which undoubtedly will accelerate the reaction kinetics and thus give a higher reaction rate. Interestingly, the Co₃O₄-6 has the highest OVs concentration, but the efficiency of Co₃O₄-6 is slightly lower than that of Co₃O₄-12. Previous studies have confirmed the interaction strength between substrate molecules and catalysts should be moderate [27,53]. The too strong interaction between catalysts and substrate molecules (such as Co₃O₄-6 system) may prolong the contact time of substrate molecules with catalysts, therefore disturbing the improvement of reaction kinetics [27,53]. While the too weak interaction between catalysts and substrate molecules is also not conducive to the improvement of catalytic efficiency owing to the feeble

adsorption and activation. The appropriate interaction between catalysts and substrate molecules not only strengthens the adsorption/activation of substrate molecules, but also shortens the contact time between substrate molecules and catalysts, thereby maximizing the reaction efficiency. As shown in Fig. 5b and c, we can find that the interaction between the Co₃O₄-12 and substrate molecules is relatively moderate compared with other samples. Therefore, the high activity of Co₃O₄-12 probably relates to the appropriate interaction with substrate molecules [27].

The reaction pathway of CO₂-to-CO conversion over the Co₃O₄-12 was investigated by in-situ diffuse reflectance infrared Fourier transform spectroscopy (DRIFTS). The peak at 2360 cm⁻¹ can be attributed to the symmetric stretching vibration modes of CO₂ (Fig. 5d and S29) [54]. The peaks from 1600 to 1750 cm⁻¹ correspond to the stretching vibration of C=O. The peaks at 1558 and 1544 cm⁻¹ can be ascribed to COOH* species [54]. The peaks at 1431 and 1329 cm⁻¹ relate to the O-H bending and C-O stretching vibration of COOH* groups, respectively [54]. It is observed that the peak of COOH* species becomes stronger with increasing the light-irradiation time, indicating that the COOH* is one of the key intermediate species for CO₂-to-CO conversion [55]. According to the DRIFTS analysis, a possible CO₂ reduction pathway is summarized in Fig. 6a.

Next, the CO₂-to-CO reduction processes over the Co₃O₄ and OV-Co₃O₄ were further explored by DFT calculations. Optimized geometric structures of various states over the Co₃O₄ and OV-Co₃O₄ along the reaction pathway are given in Figs. S30 and S31. The reaction free energy values over the Co₃O₄ and OV-Co₃O₄ are shown in Fig. 6b and Tables S8 and S9. It is seen that the CO₂ adsorption on the Co₃O₄ is slightly endothermic (0.053 eV), indicating the weak interaction between the

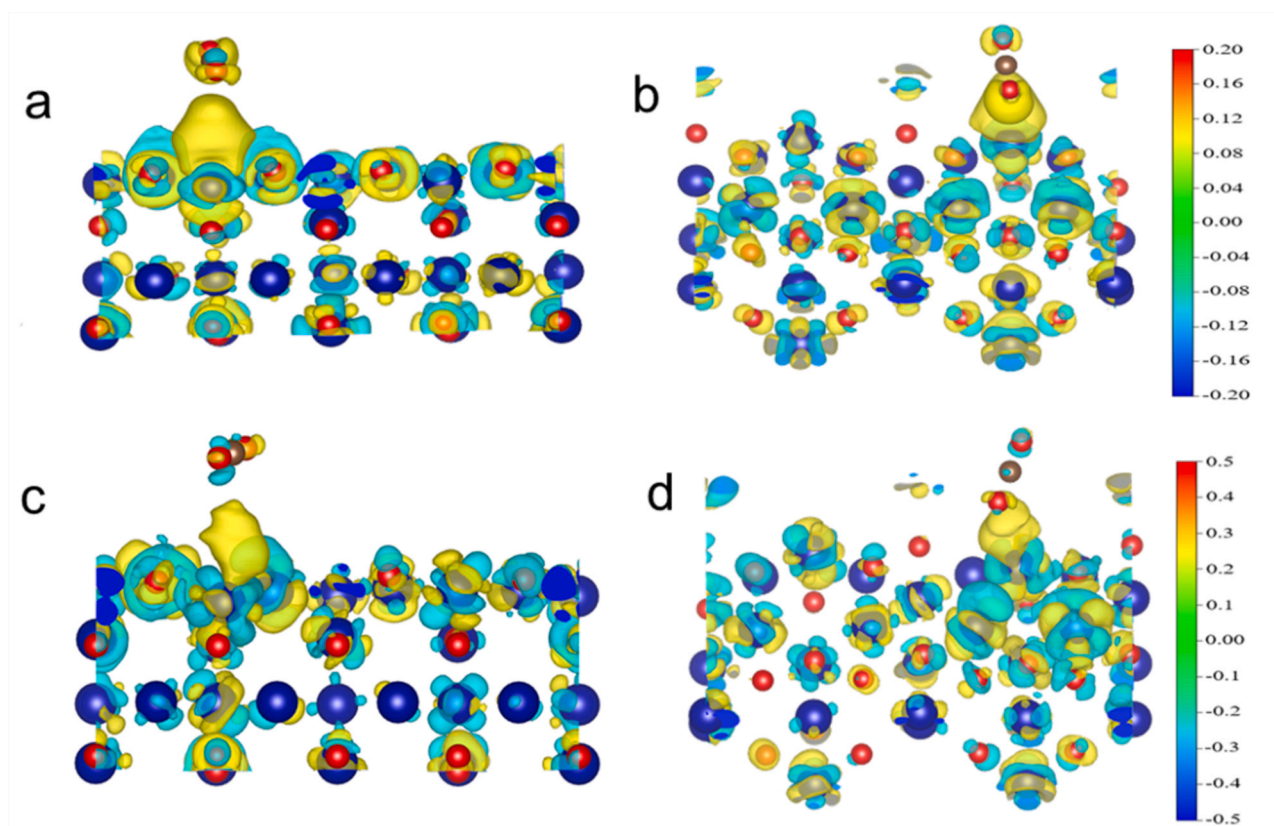


Fig. 7. Charge density difference of the CO_2 -adsorbed Co_3O_4 (a: front view, b: top view) and CO_2 -adsorbed OV- Co_3O_4 (c: front view, d: top view). The cyan and yellow indicate the regions of charge loss and gain, respectively.

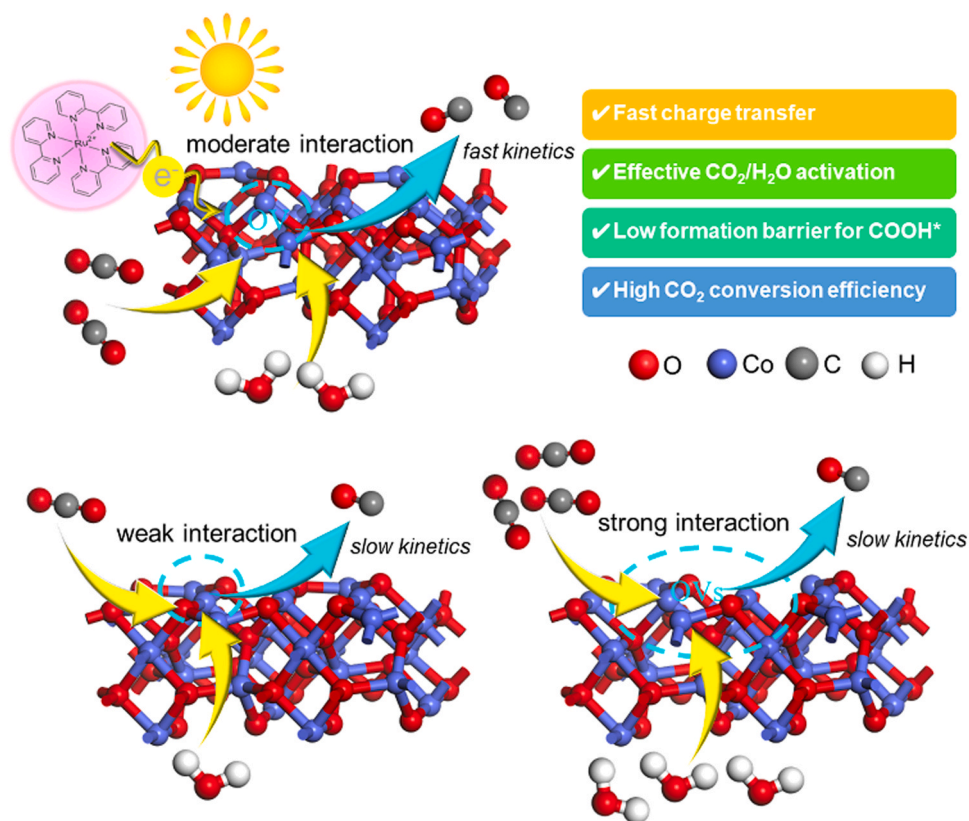


Fig. 8. Reaction mechanism of CO_2 reduction over the OV- Co_3O_4 .

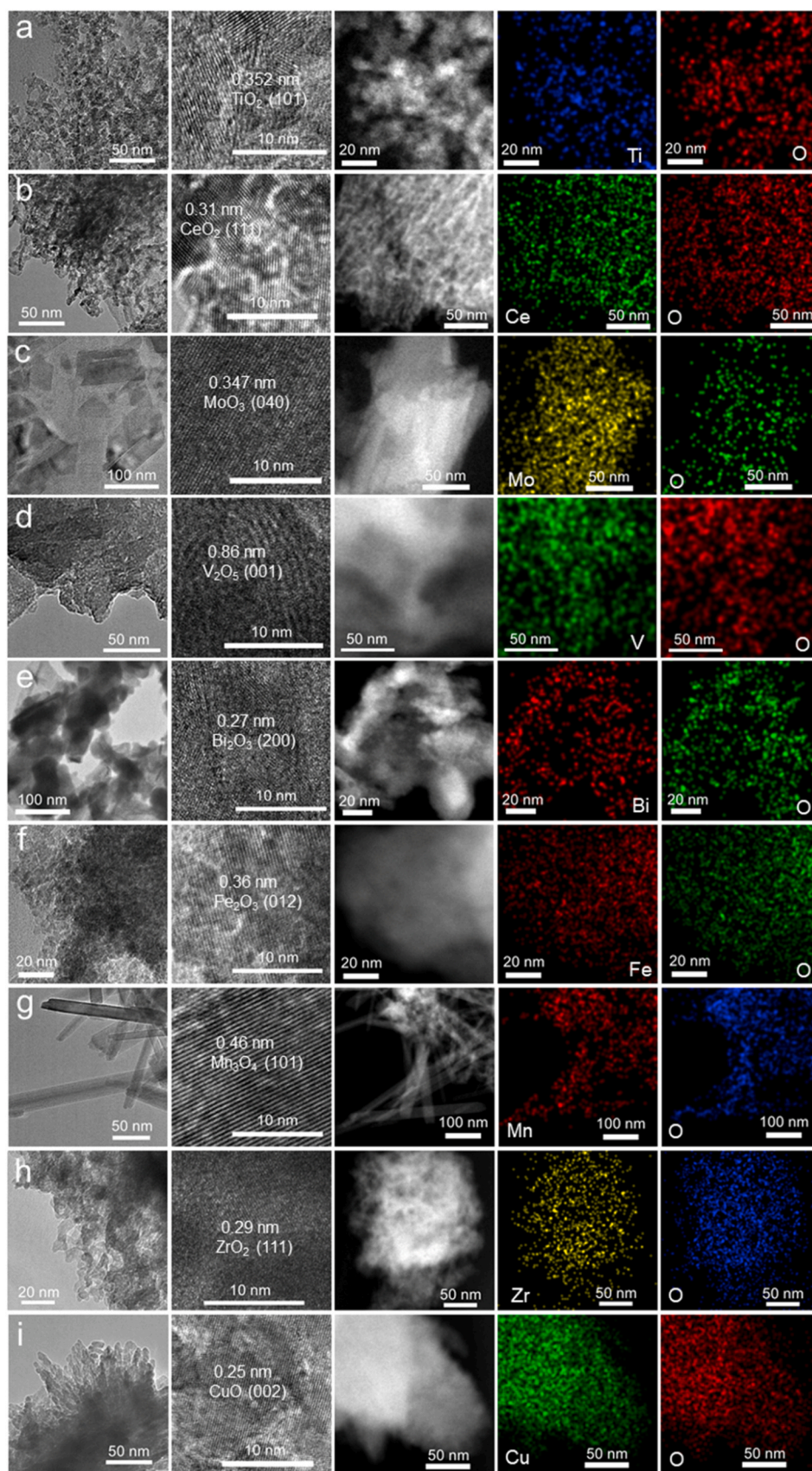


Fig. 9. Morphology characterizations of OV-rich metal oxides obtained from this photochemical methodology. TEM, HRTEM and elemental mappings of TiO_2 (a), CeO_2 (b), MoO_3 (c), V_2O_5 (d), Bi_2O_3 (e), Fe_2O_3 (f), Mn_3O_4 (g), ZrO_2 (h) and CuO (i).

Co_3O_4 and CO_2 . The formation of COOH^* and desorption of CO^* for the Co_3O_4 are highly endothermic. The free energy change (ΔG) for the formation of COOH^* and desorption of CO^* reach 0.594 and 0.685 eV, respectively. Whereas, the adsorption of CO_2 and formation of COOH^* over the OV- Co_3O_4 are exothermic. Especially, the ΔG for the formation and desorption of CO^* on the OV- Co_3O_4 are only 0.434 and 0.323 eV, respectively. By comparing the maximum ΔG values of Co_3O_4 (0.685 eV) and OV- Co_3O_4 (0.434 eV), it can be found that the CO_2 reduction over the OV- Co_3O_4 is more favourable than on the Co_3O_4 in thermodynamics.

Moreover, charge density difference was conducted to study the charge distribution on the CO_2 -adsorbed Co_3O_4 and CO_2 -adsorbed OV- Co_3O_4 . Obviously, the CO_2 -adsorbed Co_3O_4 and CO_2 -adsorbed OV- Co_3O_4 show different charge distribution (Fig. 7). The Bader charge analysis suggests that the Co atoms (Co2, Co5) adjacent OV is electron deficient compared with other Co atoms (Fig. S32, Tables S10 and S11), indicating that electrons are transferred from the Co5 and Co2 atoms to the adsorbed CO_2 . This finding reveals that the Co5 and Co2 atoms adjacent to OV are probably the key reactive sites for the activation and reduction of CO_2 .

Therefore, based on the above characterizations and DFT calculations, the excellent catalytic activity of OV- Co_3O_4 can be summarized into two key points (Fig. 8). First, the OV can inhibit recombination of the charge carriers by rapidly trapping the excited electrons of Ru dye. Second, the OV significantly modulates the electronic properties of Co_3O_4 catalysts and strengthen the interaction with substrate molecules, while greatly lowering the formation barrier for COOH^* intermediates, thereby accelerating the reaction kinetics. However, the too strong interaction between catalysts and substrate molecules (such as Co_3O_4 -6 system) can probably prolong contact time of substrate molecules with catalysts, thus impeding the enhancement of reaction kinetics to some content. Whereas, if the interaction between catalysts and substrate molecules (such as Co_3O_4 -T system) is relatively weak, the substrate molecules will not be activated efficiently, which also leads to sluggish reaction kinetics.

3.4. Generality of this photochemical synthesis strategy

Furthermore, we successfully synthesized a diverse range of OV-rich metal oxide nanocrystals by this photochemical method at ambient temperature and pressure. Fig. 9 and S33 show the TEM images of typical samples of TiO_2 , CeO_2 , MoO_3 , V_2O_5 , Bi_2O_3 , Fe_2O_3 , Mn_3O_4 , ZrO_2 and CuO prepared by this photochemical method. HRTEM characterization and elemental mappings reveal the crystalline nature and uniform element distribution of these metal oxides. XRD measurement (Fig. S34) further proves the successful synthesis of TiO_2 (PDF No.21-1272), CeO_2 (PDF No.34-0394), MoO_3 (PDF No.47-1320), V_2O_5 (PDF No.41-1428), Bi_2O_3 (PDF No.41-1449 and No.50-1088), Fe_2O_3 (PDF No.33-0664), Mn_3O_4 (PDF No.18-0803, with trace MnO_2), ZrO_2 (PDF No.49-1642) and CuO (PDF No.45-0937). Moreover, all samples demonstrate obvious OV signals (Fig. S35), reconfirming that the photochemical technique is a simple but effective approach for the synthesis of OV-rich metal oxides.

Along with the series of metal oxides mentioned above, this photochemical strategy can be further extended to prepare metal sulfides, such as MoS_2 , MnS , CdS , NiS_2 - Ni_3S_4 and Bi_2S_3 - BiS_2 (Figs. S36–S39). To explore the features of metal sulfides prepared by photochemistry, we employed MoS_2 (denoted as MoS_2 -P) as a model catalyst and studied its chemical properties and catalytic function (Figs. S40–S43). Results show that the MoS_2 -P catalyst possesses ultrathin 2D structure and rich sulfur defects. As expected, the MoS_2 -P shows enhanced activity for catalysing hydrogen evolution reaction. The hydrogen evolution rate of MoS_2 -P reaches $216.5 \mu\text{mol h}^{-1}$ under visible light irradiation, which is 15.2 times higher than that of commercial MoS_2 ($14.2 \mu\text{mol h}^{-1}$) (Figs. S43 and S44). The QY for hydrogen production over the MoS_2 -P was measured to be as high as 13% at 520 nm. Overall, we have provided a

general room-temperature photochemical route for the synthesis of defect-functioned metal oxide and metal sulfide nanocrystals, which are highly active for targeted redox reactions.

4. Conclusion

In summary, we reported a novel photochemical method for the fabrication of OV-rich Co_3O_4 nanocrystal at ambient temperature and pressure for the first time. The structural and chemical properties of OV-rich Co_3O_4 catalysts were systematically analyzed by TEM, Raman, XPS, EPR, EXAFS and PAS. As expected, the OV-rich Co_3O_4 shows excellent catalytic activity for CO_2 reduction. The TOF for Co atoms highly reaches 3.754 s^{-1} , which is one of the best reported catalysts for CO_2 photoreduction to date. Furthermore, using this photochemical strategy, we also successfully synthesized a series of defect-rich metal oxide and metal sulfide nanocrystals, which highlights its universality. We believe this novel photochemical method developed herein enriches the knowledge for the synthesis of defective nanocrystals under mild synthesis conditions and may provide new opportunity for the bottom-up approach to nanoscale fabrication in nanoscience and nanotechnology. Importantly, the intrinsic relationship between the OVs and the catalytic activity toward CO_2 reduction has been established, which will guide the rational design of efficient catalysts for CO_2 conversion and other redox reactions.

CRediT authorship contribution statement

P.Y. conceived the experiments and wrote the manuscript. Q.Z. carried out the sample synthesis, characterization and catalytic measurement. P.Y., J.Z., H.Z., Y.H. and H.Y. discussed the experimental processes. H.S. performed the DFT calculations. All the authors discussed the results.

Declaration of Competing Interest

The authors declare that they have no known competing financial interests or personal relationships that could have appeared to influence the work reported in this paper.

Acknowledgments

This work was financially supported by the National Natural Science Foundation of China (21703039, 21776168 and 21925203), Natural Science Foundation of Shanxi (201801D121044) and Science and Technology Major Project of the Shanxi Science and Technology Department (20201102005, 201903D121003, 20181102019).

Appendix A. Supporting information

Supplementary data associated with this article can be found in the online version at doi:10.1016/j.apcatb.2021.120729.

References

- [1] X. Chang, T. Wang, J. Gong, CO_2 photo-reduction: insights into CO_2 activation and reaction on surfaces of photocatalysts, *Energy Environ. Sci.* 9 (2016) 2177–2196.
- [2] K. Li, X. An, K.H. Park, M. Khraisheh, J. Tang, A critical review of CO_2 photoconversion: catalysts and reactors, *Catal. Today* 224 (2014) 3–12.
- [3] C. Gao, Q. Meng, K. Zhao, H. Yin, D. Wang, J. Guo, S. Zhao, L. Chang, M. He, Q. Li, H. Zhao, X. Huang, Y. Gao, Z. Tang, Co_3O_4 hexagonal platelets with controllable facets enabling highly efficient visible-light photocatalytic reduction of CO_2 , *Adv. Mater.* 28 (2016) 6485–6490.
- [4] L. Wang, J. Wan, Y. Zhao, N. Yang, D. Wang, Hollow multi-shelled structures of Co_3O_4 dodecahedron with unique crystal orientation for enhanced photocatalytic CO_2 reduction, *J. Am. Chem. Soc.* 141 (2019) 2238–2241.
- [5] J.H. Tu, H.H. Wu, Q.L. Qian, S.T. Han, M.G. Chu, S.Q. Jia, R.T. Feng, J.X. Zhai, M. Y. He, B.X. Han, Low temperature methanation of CO_2 over an amorphous cobalt-based catalyst, *Chem. Sci.* 12 (2021) 3937–3943.

- [6] K. Chen, H. Li, L. He, Advance and prospective on CO₂ activation and transformation strategy, *Chin. J. Org. Chem.* 40 (2020) 2195–2207.
- [7] S. Chen, H. Wang, Z. Kang, S. Jin, X. Zhang, X. Zheng, Z. Qi, J. Zhu, B. Pan, Y. Xie, Oxygen vacancy associated single-electron transfer for photofixation of CO₂ to long-chain chemicals, *Nat. Commun.* 10 (2019) 788.
- [8] G. Yin, X. Huang, T. Chen, W. Zhao, Q. Bi, J. Xu, Y. Han, F. Huang, Hydrogenated blue titania for efficient solar to chemical conversions: preparation, characterization, and reaction mechanism of CO₂ reduction, *ACS Catal.* 8 (2018) 1009–1017.
- [9] S.A. Rawool, K.K. Yadav, V. Polshettiwar, Defective TiO₂ for photocatalytic CO₂ conversion to fuels and chemicals, *Chem. Sci.* 12 (2021) 4267–4299.
- [10] S. Das, J. Perez-Ramirez, J. Gong, N. Dewangan, K. Hidajat, B.C. Gates, S. Kawi, Core-shell structured catalysts for thermocatalytic, photocatalytic, and electrocatalytic conversion of CO₂, *Chem. Soc. Rev.* 49 (2020) 2937–3004.
- [11] Z. Wei, W. Wang, W. Li, X. Bai, J. Zhao, E.C.M. Tse, D.L. Phillips, Y. Zhu, Steering electron-hole migration pathways using oxygen vacancies in tungsten oxides to enhance their photocatalytic oxygen evolution performance, *Angew. Chem. Int. Ed.* 60 (2021) 8236–8242.
- [12] G. Yang, D. Chen, H. Ding, J. Feng, J.Z. Zhang, Y. Zhu, S. Hamid, D.W. Bahnemann, Well-designed 3D ZnIn₂S₄ nanosheets/TiO₂ nanobelts as direct Z-scheme photocatalysts for CO₂ photoreduction into renewable hydrocarbon fuel with high efficiency, *Appl. Catal. B Environ.* 219 (2017) 611–618.
- [13] G. Ou, Y. Xu, B. Wen, R. Lin, B. Ge, Y. Tang, Y. Liang, C. Yang, K. Huang, D. Zu, R. Yu, W. Chen, J. Li, H. Wu, L.-M. Liu, Y. Li, Tuning defects in oxides at room temperature by lithium reduction, *Nat. Commun.* 9 (2018) 1302.
- [14] G. Wang, Y. Yang, D. Han, Y. Li, Oxygen defective metal oxides for energy conversion and storage, *Nano Today* 13 (2017) 23–39.
- [15] L. Wang, X. Xie, K.N. Dinh, Q.Y. Yan, J.M. Ma, Synthesis, characterizations, and utilization of oxygen-deficient metal oxides for lithium/sodium-ion batteries and supercapacitors, *Coord. Chem. Rev.* 397 (2019) 138–167.
- [16] Y.-M. Kim, J. He, M.D. Biegalski, H. Ambaye, V. Lauter, H.M. Christen, S. T. Pantelides, S.J. Pennycook, S.V. Kalinin, A.Y. Borisevich, Probing oxygen vacancy concentration and homogeneity in solid-oxide fuel-cell cathode materials on the subunit-cell level, *Nat. Mater.* 11 (2012) 888–894.
- [17] M.R. DeStefano, T. Islamoglu, J.T. Hupp, O.K. Farha, Room-temperature synthesis of UiO-66 and thermal modulation of densities of defect sites, *Chem. Mater.* 29 (2017) 1357–1361.
- [18] R.J. Rapf, V. Vaida, Sunlight as an energetic driver in the synthesis of molecules necessary for life, *Phys. Chem. Chem. Phys.* 18 (2016) 20067–20084.
- [19] P. Yang, R. Wang, M. Zhou, X. Wang, Photochemical construction of carbonitride structures for red-light redox catalysis, *Angew. Chem. Int. Ed.* 57 (2018) 8674–8677.
- [20] P. Yang, R. Wang, H. Zhuzhang, M.-M. Titirici, X. Wang, Photochemical construction of nitrogen-containing nanocarbons for carbon dioxide photoreduction, *ACS Catal.* 10 (2020) 12706–12715.
- [21] J.P. Perdew, K. Burke, M. Ernzerhof, Generalized gradient approximation made simple, *Phys. Rev. Lett.* 77 (1996) 3865–3868.
- [22] G. Kresse, J. Furthmüller, Efficiency of ab-initio total energy calculations for metals and semiconductors using a plane-wave basis set, *Comp. Mater. Sci.* 6 (1996) 15–50.
- [23] P.E. Blochl, Projector augmented-wave method, *Phys. Rev. B* 50 (1994) 17953–17979.
- [24] G. Kresse, D. Joubert, From ultrasoft pseudopotentials to the projector augmented-wave method, *Phys. Rev. B* 59 (1999) 1758–1775.
- [25] Hendrik Monkhorst J., James Pack D., Special points for Brillouin-zone integrations, *Phys. Rev. B* 39 (1976) 3168–3172.
- [26] B. Varghese, T.C. Hoong, Z. Yanwu, M.V. Reddy, B.V.R. Chowdari, A.T.S. Wee, T.B. C. Vincent, C.T. Lim, C.-H. Sow, Co₃O₄ nanostructures with different morphologies and their field-emission properties, *Adv. Funct. Mater.* 17 (2007) 1932–1939.
- [27] P.J. Yang, Q. Zhang, Z.L. Yi, J. Wang, H.Q. Yang, Rational electronic control of carbon dioxide reduction over cobalt oxide, *J. Catal.* 387 (2020) 119–128.
- [28] J.K. Wang, R. Gao, D. Zhou, Z.J. Chen, Z.H. Wu, G. Schumacher, Z.B. Hu, X.F. Liu, Boosting the electrocatalytic activity of Co₃O₄ nanosheets for a Li-O₂ battery through modulating inner oxygen vacancy and exterior Co³⁺/Co²⁺ ratio, *ACS Catal.* 7 (2017) 6533–6541.
- [29] Z. Cai, Y. Bi, E. Hu, W. Liu, N. Dwarica, Y. Tian, X. Li, Y. Kuang, Y. Li, X.-Q. Yang, H. Wang, X. Sun, Single-crystalline ultrathin Co₃O₄ nanosheets with massive vacancy defects for enhanced electrocatalysis, *Adv. Energy Mater.* 8 (2018), 1701694.
- [30] L. Xu, Q. Jiang, Z. Xiao, X. Li, J. Huo, S. Wang, L. Dai, Plasma-engraved Co₃O₄ nanosheets with oxygen vacancies and high surface area for the oxygen evolution reaction, *Angew. Chem. Int. Ed.* 55 (2016) 5277–5281.
- [31] F. Wang, S. Bai, W. Tress, A. Hagfeldt, F. Gao, Defects engineering for high-performance perovskite solar cells, *NPJ Flex. Electron.* 2 (2018) 22.
- [32] Y.-C. Zhang, Z. Li, L. Zhang, L. Pan, X. Zhang, L. Wang, A. Fazal e, J.-J. Zou, Role of oxygen vacancies in photocatalytic water oxidation on ceria oxide: experiment and DFT studies, *Appl. Catal. B Environ.* 224 (2018) 101–108.
- [33] S. Yang, Y. Liu, Y. Hao, X. Yang, W.A. Goddard III, X.L. Zhang, B. Cao, Oxygen-vacancy abundant ultrafine Co₃O₄/graphene composites for high-rate supercapacitor electrodes, *Adv. Sci. (Weinh.)* 5 (2018), 1700659.
- [34] Z. Xiao, Y. Wang, Y.-C. Huang, Z. Wei, C.-L. Dong, J. Ma, S. Shen, Y. Li, S. Wang, Filling the oxygen vacancies in Co₃O₄ with phosphorus: an ultra-efficient electrocatalyst for overall water splitting, *Energy Environ. Sci.* 10 (2017) 2563–2569.
- [35] H. Zhang, Z. Wang, C. Ma, Z. Zhou, L. Cao, J. Yang, Regulating the coordination of Co sites in Co₃O₄/MnO₂ compounding for facilitated oxygen reduction reaction, *ChemSusChem* 13 (2020) 6613–6620.
- [36] X.D. Jiang, Y.P. Zhang, J. Jiang, Y.S. Rong, Y.C. Wang, Y.C. Wu, C.X. Pan, Characterization of oxygen vacancy associates within hydrogenated TiO₂: a positron annihilation study, *J. Phys. Chem. C* 116 (2012) 22619–22624.
- [37] M. Guan, C. Xiao, J. Zhang, S. Fan, R. An, Q. Cheng, J. Xie, M. Zhou, B. Ye, Y. Xie, Vacancy associates promoting solar-driven photocatalytic activity of ultrathin bismuth oxychloride Nanosheets, *J. Am. Chem. Soc.* 135 (2013) 10411–10417.
- [38] X. Hu, T. Koyanagi, Y. Katoh, B.D. Wirth, Positron annihilation spectroscopy investigation of vacancy defects in neutron-irradiated 3C-SiC, *Phys. Rev. B* 95 (2017), 104103.
- [39] S. Szpala, P. AsokaKumar, B. Nielsen, J.P. Peng, S. Hayakawa, K.G. Lynn, H. J. Gossman, Defect identification using the core-electron contribution in Doppler-broadening spectroscopy of positron-annihilation radiation, *Phys. Rev. B* 54 (1996) 4722–4731.
- [40] M. Kong, Y. Li, X. Chen, T. Tian, P. Fang, F. Zheng, X. Zhao, Tuning the relative concentration ratio of bulk defects to surface defects in TiO₂ nanocrystals leads to high photocatalytic efficiency, *J. Am. Chem. Soc.* 133 (2011) 16414–16417.
- [41] C.-H. Wu, J.-M. Chern, Kinetics of photocatalytic decomposition of methylene blue, *Ind. Eng. Chem. Res.* 45 (2006) 6450–6457.
- [42] H.T. Luk, C. Mondelli, D.C. Ferre, J.A. Stewart, J. Perez-Ramirez, Status and prospects in higher alcohols synthesis from syngas, *Chem. Soc. Rev.* 46 (2017) 1358–1426.
- [43] A. Li, T. Wang, X. Chang, Z.-J. Zhao, C. Li, Z. Huang, P. Yang, G. Zhou, J. Gong, Tunable syngas production from photocatalytic CO₂ reduction with mitigated charge recombination driven by spatially separated cocatalysts, *Chem. Sci.* 9 (2018) 5334–5340.
- [44] J. Schneider, H. Jia, J.T. Muckerman, E. Fujita, Thermodynamics and kinetics of CO₂, CO, and H⁺ binding to the metal centre of CO₂ reduction catalysts, *Chem. Soc. Rev.* 41 (2012) 2036–2051.
- [45] A. Goyal, G. Marcandalli, V.A. Mints, M.T.M. Koper, Competition between CO₂ reduction and hydrogen evolution on a gold electrode under well-defined mass transport conditions, *J. Am. Chem. Soc.* 142 (2020) 4154–4161.
- [46] X.C. Wang, K. Maeda, A. Thomas, K. Takanabe, G. Xin, J.M. Carlsson, K. Domen, M. Antonietti, A metal-free polymeric photocatalyst for hydrogen production from water under visible light, *Nat. Mater.* 8 (2009) 76–80.
- [47] X.C. Wang, X.F. Chen, A. Thomas, X.Z. Fu, M. Antonietti, Metal-containing carbon nitride compounds: a new functional organic-metal hybrid material, *Adv. Mater.* 21 (2009) 1609–1612.
- [48] J.S. Zhang, M.W. Zhang, R.Q. Sun, X.C. Wang, A facile band alignment of polymeric carbon nitride semiconductors to construct isotype heterojunctions, *Angew. Chem. Int. Ed.* 51 (2012) 10145–10149.
- [49] K.-Q. Lu, Y.-H. Li, F. Zhang, M.-Y. Qi, X. Chen, Z.-R. Tang, Y.M.A. Yamada, M. Anpo, M. Conte, Y.-J. Xu, Rationally designed transition metal hydroxide nanosheet arrays on graphene for artificial CO₂ reduction, *Nat. Commun.* 11 (2020) 5181.
- [50] R. Shi, Y. Zhao, G.I.N. Waterhouse, S. Zhang, T. Zhang, Defect engineering in photocatalytic nitrogen fixation, *ACS Catal.* 9 (2019) 9739–9750.
- [51] X.Z. Fu, L.A. Clark, W.A. Zeltner, M.A. Anderson, Effects of reaction temperature and water vapor content on the heterogeneous photocatalytic oxidation of ethylene, *J. Photoch. Photobio. A* 97 (1996) 181–186.
- [52] P.J. Yang, H.Y. Zhuzhang, R.R. Wang, W. Lin, X.C. Wang, Carbon vacancies in a melon polymeric matrix promote photocatalytic carbon dioxide conversion, *Angew. Chem. Int. Ed.* 58 (2019) 1134–1137.
- [53] Q. Cheng, Y. Tian, S. Lyu, N. Zhao, K. Ma, T. Ding, Z. Jiang, L. Wang, J. Zhang, L. Zheng, F. Gao, L. Dong, N. Tsubaki, X. Li, Confined small-sized cobalt catalysts stimulate carbon-chain growth reversibly by modifying ASF law of Fischer-Tropsch synthesis, *Nat. Commun.* 9 (2018) 3250.
- [54] P. Yang, R. Wang, H. Tao, Y. Zhang, M.-M. Titirici, X. Wang, Cobalt nitride anchored on nitrogen-rich carbons for efficient carbon dioxide reduction with visible light, *Appl. Catal. B Environ.* 280 (2021), 119454.
- [55] Y. Fang, X. Wang, Photocatalytic CO₂ conversion by polymeric carbon nitrides, *Chem. Commun.* 54 (2018) 5674–5687.